

Simulation of surface x-ray emission from the ASTERICS ECR ion source

T. Thuillier,¹ A. Cernuschi,¹ and B. Cheymol¹*Université Grenoble Alpes, CNRS-LPSC, INP Grenoble, Grenoble, France*

(*Electronic mail: thomas.thuillier@lpsc.in2p3.fr.)

(Dated: 9 July 2025)

The bremsstrahlung x-ray emission induced by the impact of plasma electrons de-confined on the chamber wall of the ASTERICS electron cyclotron resonance ion source is investigated through a suite of two simulation codes. The electron high energy temperature distribution tail at the wall is found to be anisotropic and increases with B_{min} . The electrons impinge the walls with broad angular distribution peaking at angles ranging between 5-25° with respect to the surface, which has consequences on the x-ray emission directionality and on the yield of electrons bouncing back toward the plasma, reaching up to 50%. The x-ray dose is mapped inside and around the ion source for $B_{min} = 0.8$ T and an electron temperature artificially increased to 120 keV to dimension with margin the cave shielding. The dose without shielding reaches $100 \mu\text{Sv h}^{-1}$ per kW of impacting electrons at 5 m. A set of internal and external shielding is presented to attenuate this dose and reduce it to less than $1 \mu\text{Sv h}^{-1}$ per kW of electrons. A parametric electron distribution temperature study with Fluka indicates that the deposition of 1 W of heat in the superconducting cold mass per kW of plasma electrons, as reported experimentally, is obtained when the temperature is set to 380 keV. The mechanism required to provide such a high electron temperature is unclear, but previous experiments on several ion sources reported an x-ray spectral temperature 3 to 4 times higher radially, compatible with this simulation result.

I. ELECTRON LOSSES TO THE WALL

A. Model and methodology

An existing Monte-Carlo (MC) code was adapted to study the electron dynamics inside the ASTERICS ion source plasma chamber^{1,2}, currently under design (see the overall source cutaway view on Fig. 1). The 28 GHz radio-frequency (RF) electric field considered in the simulation is modeled with a transverse traveling plane wave with a circular polarization and a constant electric field intensity $E = 10 \text{ kV m}^{-1}$ (corresponding to 7 kW of injected RF power). An argon plasma is assumed with a mean ion charge state of ~ 8 . The plasma density considered is 15 % of the cut-off density at 28 GHz. The ions are considered frozen in the cavity. The initial electron energies are randomly sampled using a set of Gaussian distributions centered on each argon ionization potential energies (IP) with a standard deviation of $10\% \times \text{IP}$, with a relative abundance following a typical argon ion spectrum. The electrons undergo Coulomb collision and electron impact with ions. The RF pitch angle³ scattering is not considered in the simulation, in order to maximize the electrons energy and the associated high energy bremsstrahlung emission. The electrons are tracked until they impact the 3 possible walls: injection at $z_{inj} = 0.3$ m, extraction at $z_{ext} = -0.3$ m and radial wall at $r_w = 0.091$ m. Two static electric fields are modeled in the MC simulation. One for the injection biased disk with a voltage of -100 V and a diameter of 20 mm. The second for the accelerating electric field of the ion source on the extraction, being 10 kV cm^{-1} , extending for 4 cm right after the extraction electrode hole of 10 mm diameter. The electrons having a propagation time larger than 1 ms (this time being 3-4 times larger than the mean electrons confinement time simulated) are considered highly confined and are stopped. A set of 1.25×10^6 electrons was simulated for each magnetic configuration. The electron final positions and velocities on the plasma chamber wall were stored and analyzed. The electron

particle distribution at the plasma chamber wall was studied for two axial magnetic field configurations: 3.7-0.3-2.2 T and 3.7-0.8-2.2 T, deemed representative of the actual ion source operation. The hexapolar radial magnetic field intensity at wall is fixed at 2.4 T. The $B_{min} = 0.3$ T configuration, suitable for double frequency operation (18+28 GHz), is known to generate a low output flux of energetic x-rays⁴. On the contrary, the $B_{min} = 0.8$ T configuration experimentally maximises the production of high energy x-rays⁴⁻⁶. The aforementioned magnetic configurations are used to probe the minimum and maximum x-ray dose in the accelerator cave, respectively.

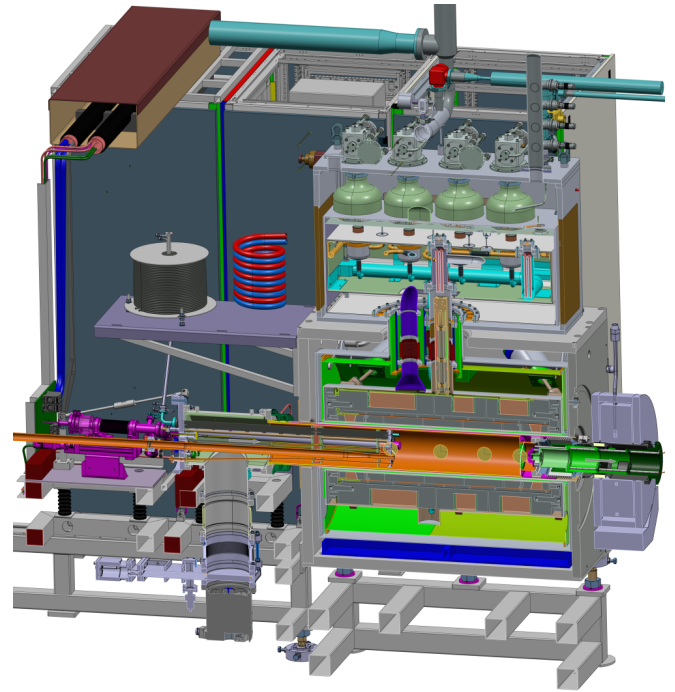


FIG. 1. Cutaway view of the ASTERICS ion source design.

B. Monte-Carlo Results

The electron energy distribution function (EEDF) of the electrons impacting the walls are plotted in Fig. 2(a) and Fig. 2(b) for the magnetic configurations $B_{min} = 0.3$ and 0.8 T respectively. The EEDF for the injection, radial and extraction walls are reported in each subplot in black, blue and red respectively. For completeness, the EEDF of electrons still confined in the source volume after 1 ms are indicated in cyan. This specific electron population is expected to contribute to the volume plasma bremsstrahlung emission which is not studied here. The high energy part of each EEDF population have been fitted with a Maxwell-Boltzmann distribution, and the temperature obtained, expressed in keV, are reported in the Tab. I for each surface and magnetic configuration and for the electron still confined after 1 ms. The EEDF is found to vary both on the wall surface location and with B_{min} . The normalized counts per wall surface associated with $B_{min} = 0.3$ and 0.8 T are proposed in Tab. II. One can note a transfer of the flux of electrons from the radial wall (76 to 52 %) to the extraction wall (17 to 41 %) when B_{min} is changed from 0.3 to 0.8 T. The reason for this shift is a change of the minimum magnetic field intensity at the plasma chamber wall, which passes from 2.03 to 2.29 T, making the weakest magnetic point the extraction peak field (2.2 T) for the latter case. The increase of B_{min} is coming along with a temperature increase of the hot electrons (T_{rad} from 41 to 52 keV, T_{ext} from 44 to 63 keV). This specific topic will be discussed in another paper dedicated to the ASTERICS plasma x-ray volume emission⁷. It is also worth noting that, for $B_{min} = 0.8$ T, the three EEDF feature a visible hump for $E \approx 15$ -20 keV, which is known to cause plasma instabilities and has been confirmed experimentally for such a high B_{min} ⁸. Figure 3 presents the distribution of angle of incidence θ of electrons hitting the plasma chamber wall ($\theta = (\vec{v}, \vec{n})$, \vec{n} local normal to the surface) for (a) $B_{min} = 0.3$ T and (b) 0.8 T. The color plot convention in Fig. 3 is identical to the one adopted in Fig. 2. One can observe how the magnetic field intensity strongly influences the distribution shape. While the distributions for the injection are almost identical for (a) and (b), one can observe a stronger peaking of the extraction wall distribution when B_{min} is increased from 0.3 to 0.8 T, with a most probable angle of $\approx 85^\circ$. On the other hand, a concomitant reduction of the most probable impact angle at the radial wall is found, from 72° to 65° . The high values of θ are a consequence of the magnetic mirror effect (pitch angle loss cone) and the concomitant accumulation of perpendicular electron energy by the ECR mechanism. The direction of impact of electrons on the wall influences the direction of emission of bremsstrahlung photons and must be considered in the bremsstrahlung simulation. The electron distribution on the injection, radial and extraction wall is proposed for $B_{min} = 0.3$ and 0.8 T in Fig. 4. While the electron distribution is marginally affected on the injection surface (with nevertheless a triangular core centered on the axis which is twice as large as the case when $B_{min} = 0.8$ T), one can observe how the distribution is significantly re-balanced between the radial and the extraction walls. At $B_{min} = 0.8$ T, the radial electron distribution is concentrated on a much smaller

surface, while the place where high flux of electron hits the extraction wall is largely enhanced.

TABLE I. Estimation of the EEDF high energy tail temperature obtained on the injection (T_{inj}), radial (T_{rad}) and extraction plasma chamber walls (T_{ext}) for the two cases $B_{min} = 0.3$ and 0.8 T. T_{conf} corresponds to the temperature of the electrons still confined after 1 ms.

Axial profile (T)	T_{inj} (keV)	T_{rad} (keV)	T_{ext} (keV)	T_{conf} (keV)
3.7-0.3-2.2	19.8 ± 1.6	41.7 ± 1.5	44.0 ± 7.4	39.2 ± 1.5
3.7-0.8-2.2	36.0 ± 8.6	52.0 ± 3.1	63.2 ± 7.9	89.2 ± 1.6

TABLE II. Distribution of the final position of the electrons for the two magnetic axial profiles considered. The subscripts $\%inj$, $\%ext$ and $\%rad$ refer respectively to the particles deconfined at the injection, extraction and radial walls. $\%conf$ stands for the amount of electrons still confined at the time limit of 1 ms.

Axial profile	$\%inj$	$\%ext$	$\%rad$	$\%conf$
3.7-0.3-2.2 T	3.2	17.3	76.0	3.6
3.7-0.8-2.2 T	5.8	41.5	52.1	0.6

TABLE III. Total x-ray photon to electron yield passing through the injection, radial and extraction wall surfaces, for $B_{min} = 0.3$ and 0.8 T.

Axial profile	photon / e^-	$\%inj$	$\%rad$	$\%ext$
3.7-0.3-2.2 T	$5.7 \cdot 10^{-5}$	15 %	60 %	25 %
3.7-0.8-2.2 T	$1.6 \cdot 10^{-4}$	27 %	11 %	62 %

II. FLUKA SIMULATION

A. Geometrical model and methodology

A simplified three dimensions version of the ASTERICS ion source geometry and the first meter of its low energy beam transfer line (LEBT) have been modeled with Fluka⁹. A sectional view of the Fluka model is proposed in Fig. 5. The ion source model includes the actual geometry of the superconducting magnet cold mass¹⁰, the source iron yoke, the plasma chamber, representative components of the atom and RF injection system (two oven ports and one 28 GHz oversized waveguide) and the ion extraction electrodes. The LEBT model includes the elements located on the ion source axis: the beam pipes, a vacuum chamber, the first two solenoids and a 90° bending magnet. The Fluka model also includes the actual ion source cave geometry whose walls are made up with concrete. The Fluka model is completed with a set of shields located at specific places to damp the bremsstrahlung emission induced by the impact of electrons on the plasma chamber surface. The shield locations and their thicknesses are indicated in Fig. 5. The goal of these added shields is

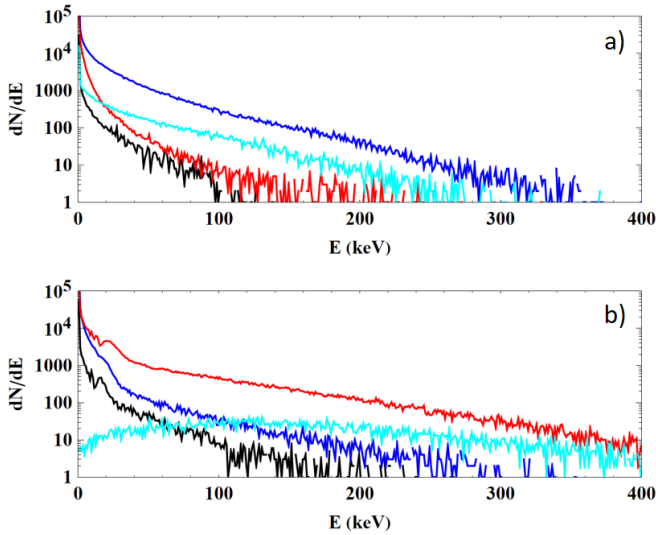


FIG. 2. EEDF of the electrons hitting the plasma chamber wall for (a) $B_{min} = 0.3$ T and (b) $B_{min} = 0.8$ T. The black, blue and red plots are respectively recorded on the injection ($z=z_{inj}$), radial ($r=r_{wall}$) and extraction surfaces ($z=z_{ext}$). The cyan EEDF plots corresponds to the electron still confined in the plasma chamber volume after 1 ms.

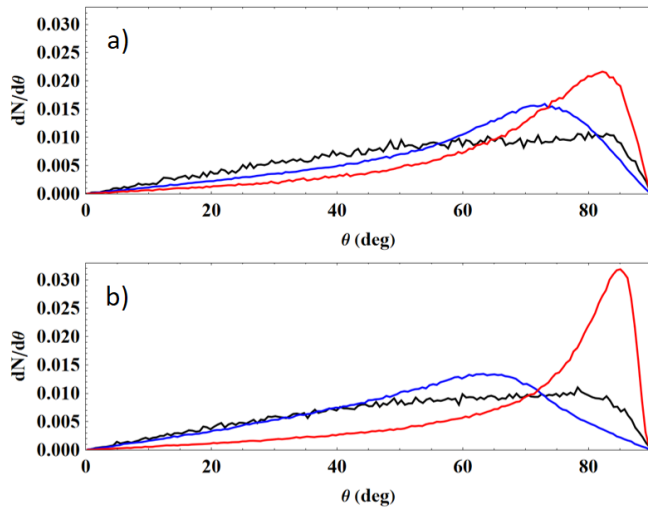


FIG. 3. Distribution of the angle of incidence of electron impacting the plasma chamber walls ($\theta = (\vec{v}, \vec{n})$, \vec{n} normal to the surface) (a) for $B_{min} = 0.3$ T and (b) for $B_{min} = 0.8$ T. The black, blue and red curves correspond to the injection, radial and extraction surfaces respectively.

to mitigate the dose around the ion source, allowing the safe circulation of personnel in a corridor located next to the ion source, with a maximum dose rate of $7.5 \mu\text{Sv h}^{-1}$. The output of the MC electron simulation (position and velocity direction) is used as an input for the Fluka code, while the EEDF is assumed to follow a Maxwell-Boltzmann distribution with a chosen temperature. The MC results for $B_{min} = 0.3$ T with an EEDF temperature fixed to 50 keV are used to study a typical operation which minimizes the x-ray dose emitted from

the source. The MC results for $B_{min} = 0.8$ T are used to study the case of high bremsstrahlung x-ray flux in operation and dimension the x-ray shieldings necessary for the safe ion source operation and in the cave. For $B_{min} = 0.8$ T, the EEDF temperature is set to 120 keV, a value 20 % higher than the measured experimental axial x-ray spectral temperature in similar ion sources⁴⁻⁶, deemed conservative for this study. A specific volume, modeled by an argon gas, is included in the plasma chamber to manage specifically the electrons bouncing back from the chamber walls toward the plasma. Indeed, for computation time reason, the source magnetic field is not included in the Fluka simulation and the straight trajectories of reflected electrons passing through the plasma chamber volume are consequently not realistic. Thus, an electron going back toward the plasma is considered as re-absorbed by the plasma and is stopped in the Fluka simulation. Because electrons are magnetized and approximately follow magnetic field lines in ECRIS, such a stopped electron is implicitly taken into account by starting a fresh new electron hitting the plasma chamber wall according to the MC output distribution. On the other hand, the secondary photons emitted backward toward the plasma can propagate freely through the gas volume, with a very small probability of interaction, like for crossing a plasma. Each of the three plasma chamber surface (injection disk, radial cylinder and extraction disk) that electrons hit is used to start an independent Fluka simulation. This allows in particular to investigate the secondary photon directionality. The 3 simulations results are next merged to obtain the full x-ray spectrum of the ion source.

B. X-ray flux exiting the source and shielding scaling

In Fluka, the secondary particles showers (mainly photons and electrons) generated by each primary electron are followed until they are fully stopped by matter. Because of the small angle between the initial electron directions and the impacted surface, it is found that approximately 50 % of the electrons are bouncing back toward the plasma. Such a high reflection rate is likely to increase the actual electron confinement time in ECRIS. Figure 6 presents the x-ray fluence per electron impinging (a) the injection surface, (b) the radial surface and (c) the extraction surface when B_{min} and T_e are 0.8 T and 120 keV respectively. One can see that the dominant x-ray photon leak able to exit the source occurs on the source injection side, at the place where the material thickness is the lowest. Being mainly composed of a thick layer of stainless steel, soft iron, Nb-Ti and copper, the superconducting magnet cold mass efficiently stops the radial photon flux in the first radial centimeters. The 5 cm thick iron yoke surrounding the superconducting magnet cryostat also strongly attenuates the x-ray flux passing through it. On the other hand, the x-rays exiting on the extraction side are either directed along the beam pipe axis or channeled radially in the gap between the source and the first focusing solenoid yoke. Table III presents the total x-ray yield per electron generated for $B_{min}/T_e = 0.3$ T / 50 keV and 0.8 T / 120 keV respectively. The increase of B_{min} from 0.3 to 0.8 T favors the leak of photons toward the injection

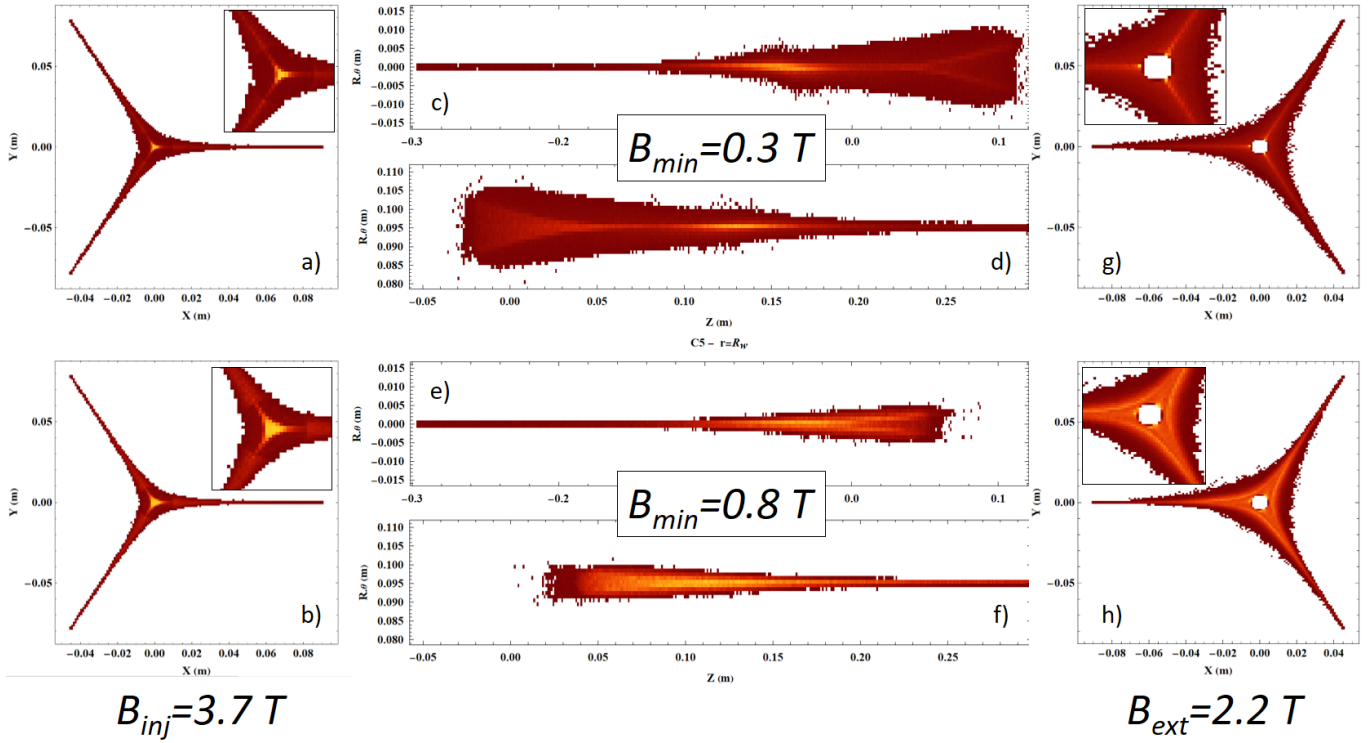


FIG. 4. Electron density distribution at the injection ((a) and (b)), radial ((c), (d), (e) and (f)) and extraction ((g) and (h)) surface of the plasma chamber wall for $B_{min} = 0.3 T$ (top plots) and $B_{min} = 0.8 T$ (bottom plots). The dimension scale of images between the top and the bottom is conserved.

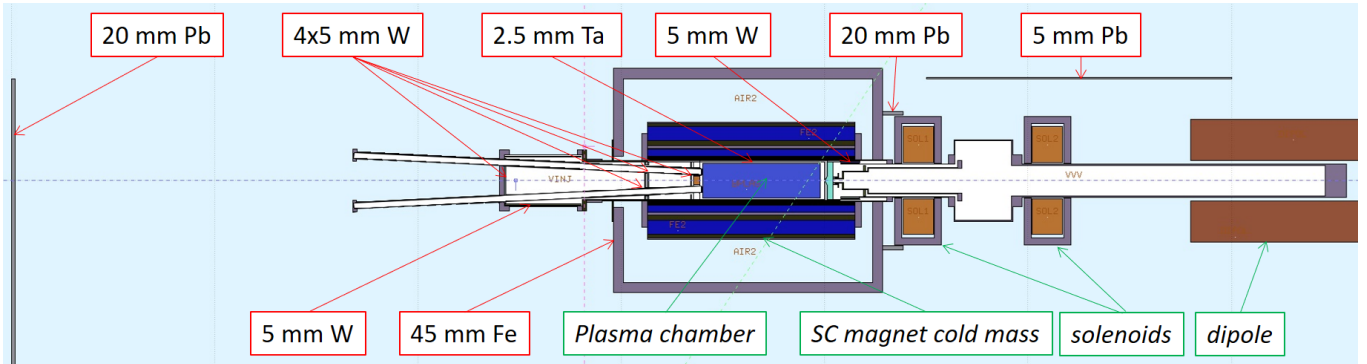


FIG. 5. Sectional view of the ion source geometry modeled with Fluka. Detail of the materials thickness used to shield the x-ray emission from the source are provided. See text for details.

and extraction walls (27 % and 62 % respectively) rather than the radial direction (11 % only). This effect is likely a consequence of the following facts: (i) an increase of the electron yield on the extraction wall for $B_{min} = 0.8 T$ (see Tab. II), (ii) a high rate of electrons bouncing on the radial walls and (iii) x-ray traversing thick material layers are subject to diffusion and back-scattering, favoring the remaining photons to escape toward the directions with lesser matter (injection and extraction). Indeed, Fluka propagates all the secondary particles generated by the incident electrons until the particle shower ends. The yields presented in Tab. III also include numerous lower energy photons subject to high scattering prob-

ability, which would finally not be detected outside of the ion source. The dose around the source in the cave, when no specific shielding is present, is displayed in Fig 7(a). The local dose is as high as $100 \mu\text{Sv h}^{-1}$ per kW of injected electrons in the corridor located on the left ($z < -600$ cm) of the ion source, on its injection side. In order to damp the dose rate below the allowed $7.5 \mu\text{Sv}$ limit in the corridor, specific shieldings were added and their effect investigated with Fluka (see Fig. 5). In order to reduce the need of bulky shielding outside of the ion source on the injection side, a set of four 5 mm thick tungsten screens are placed under vacuum as close as possible from the x-ray emission, behind the plasma injection flange, as can be

seen in Fig. 5 and 8. The shields are hollowed by a set of three 40 mm diameter holes, to model the passage of the two metallic oven ports and the over-sized 28 GHz waveguide. The lack of matter inside these tubes is expected to channel x-rays out of the source and their effect had to be investigated. It is found that an extra layer of 20 mm of lead is required to shield the rear part of the source atom and RF injection system. This shield dimension is limited to a small solid angle and is located far away from the place where the daily maintenance of the source is done. Finally, a 5 mm thick lead shield is fixed along the fences closing the ion source high voltage zone (see the vertical line on the left of the source in Fig. 7b). On the extraction side, the x-rays are blocked by a 5 mm thick tungsten cylinder located around the extraction system and by a 20 mm thick lead cylinder closing the radial gap between the source yoke and the extraction solenoid yoke. The resulting x-ray dose after filtering is displayed in Fig. 7(b), showing only places where the dose is higher than $5 \mu\text{Sv h}^{-1}$ per kW of electrons. One can check that the modeled compact shielding efficiently screens the x-ray and prevent the dose to extend outside of the cave. The mean dose in the corridor on the left is lower than $1 \mu\text{Sv h}^{-1}$.

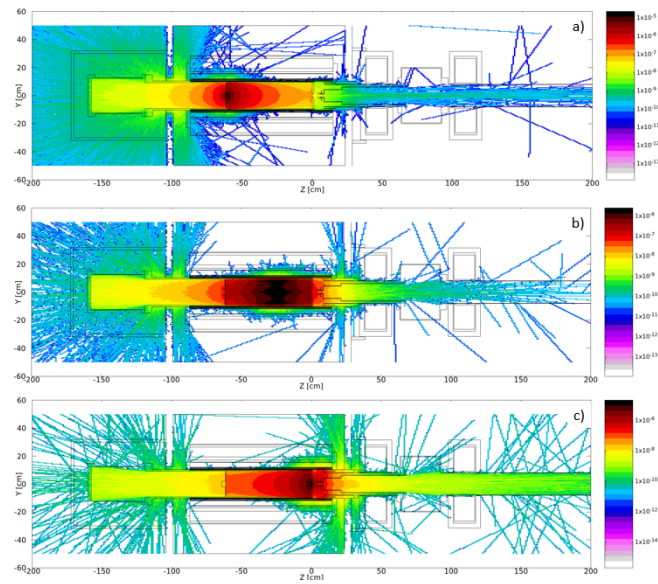


FIG. 6. Averaged x-ray fluence generated by the impact of a single electron on injection (a), radial (b), and extraction walls (c) when $B_{min} = 0.8 \text{ T}$ and $T_e = 120 \text{ keV}$.

C. X-ray power to the magnet cold mass

The return of experience from the 3rd generation ECRIS operation at 28 GHz shows a parasitic heating of the superconducting magnet cold mass caused by the x-ray flux generated by electron bremsstrahlung impacting the plasma chamber walls. This heat load is linearly increasing with B_{min} and values up to 1 W of extra heat load per kW of injected RF have been reported¹¹. Fluka is used to investigate the power

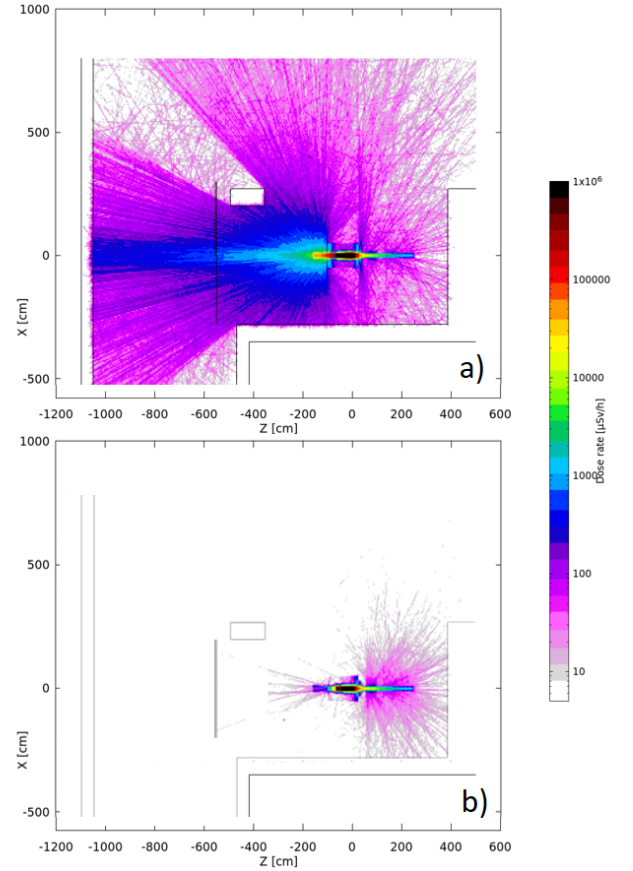


FIG. 7. X-ray dose per kW of electron simulated in the cave (a) without and (b) with shielding when $B_{min} = 0.8 \text{ T}$ and $T_e = 120 \text{ keV}$.

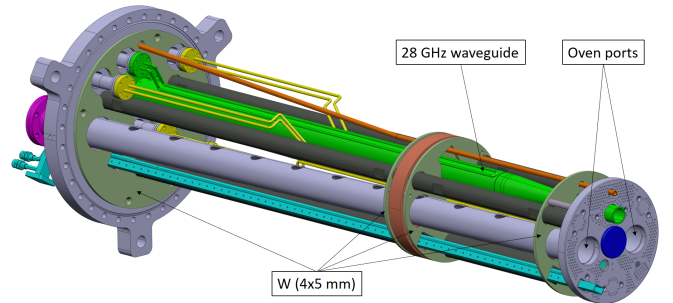


FIG. 8. View of the ion source injection system mechanics showing the 4 tungsten screens located under vacuum and the two specific ports modeled in Fluka: the two oven ports and the 28 GHz over-sized waveguide.

deposited into the cryostat as a function of the EEDF temperature. The electron initial direction corresponding to the case $B_{min} = 0.8 \text{ T}$ were used. The Maxwell-Boltzmann EEDF temperature was varied from 50 keV to 500 keV. A set of 10^9 electrons were cast in Fluka to obtain a sufficient statistic to investigate the power deposited in the cold mass per kW of impinging electrons to the plasma chamber wall. The resulting power is plotted in Fig. 9. One can see that the EEDF temperature necessary to deposit 1 W per kW of electrons is

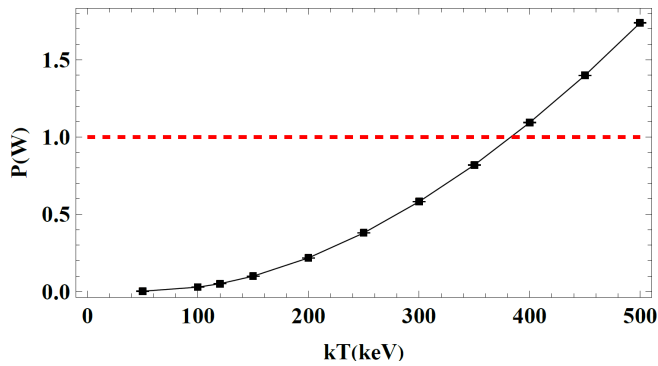


FIG. 9. Evolution of the total power deposited to the source cold mass (per kW of incident electrons) as a function of the EEDF temperature impinging the plasma chamber walls (black solid line). The 1 W level observed experimentally is indicated with a red dashed line.

$T \approx 380$ keV. This value is 3 to 4 times higher than the x-ray spectral temperature experimentally measured on 3rd Generation ECRIS along the source axis^{5,6,11}, suggesting an important temperature anisotropy in those ECRIS. This very high radial electron temperature obtained by Fluka was unexpected and the physics mechanism necessary to produce such a high temperature EEDF is unclear to the authors. Nevertheless, it is worth mentioning that high spectral temperature anisotropy has been experimentally reported with two distinct ECRIS having a (rare) direct radial view to the plasma. First with the Quadrupafios ion source, where the radial spectral temperature was measured up to 230 keV, while the axial one was ≈ 90 keV for a plasma heated at 18 GHz^{12,13}. And second, with the AECS source heated at 14+12.5 GHz which revealed a radial spectral temperature of 100 keV, while the axial one was 30 keV¹⁴.

III. CONCLUSION

The x-ray dose exiting the ASTERICS ion source, induced by the impact of plasma electrons on the plasma chamber wall, has been studied with Fluka, using as input the results of a MC electron code simulating the hot electron dynamics in the ECRIS. The MC code results indicate an important spatial electron temperature anisotropy at the three plasma chamber walls (injection disk, radial cylinder and extraction disk). An increase of the electron temperature at the three walls is obtained when B_{min} increases. The distribution of electron flux to these surfaces is also found to be strongly dependent on the value of B_{min} : the electron flux leaks preferentially toward the place where the magnetic field is minimum. This behavior is a consequence of the electron Coulomb scattering model used in the plasma. The distributions of angle of incidence of the electrons with respect to the normal to the local surface present a peak above 60° and 80° for the radial and extraction walls respectively. These distribution angles are a consequence of the magnetic mirroring effect happening in the strongly magnetized ECRIS, which favors the confinement

of electrons heated by the ECR mechanism and hence characterized by large perpendicular velocities. The large angle of incidence of electron to the wall results in a large amount of them ($\approx 50\%$) being bounced back toward the plasma. It also results in specific solid angles of photon emissions that must be considered to appropriately simulate the x-ray spatial emission distribution from ECRIS. Without shielding, a dose higher than $\sim 100 \mu\text{Sv h}^{-1}$ per kW of primary electrons is obtained in the corridor located at a distance of 5 m from the injection side of the ECRIS in the NEWGAIN cave. A shielding composed of four 5 mm plates of tungsten placed inside the source, under vacuum and as close as possible to the plasma chamber, is used to attenuate the x-ray dose emitted on the source injection side. This solution allows reducing dramatically the places where x-ray shielding must be placed around the ECRIS, resulting in a simplified ion source maintenance and a simpler and cheaper radiation safety design. A parametric EEDF temperature study done with Fluka finds that the electron temperature required to heat the ion source superconducting magnet cold mass up to 1 W per kW of primary electrons, level of power measured experimentally, is 380 keV. Such a high temperature is found neither with MC simulations nor by experimental photon spectral temperature axial measurements ($T_S \leq 100$ keV), but this result is consistent with experimental spectral temperature anisotropy measured in two different ECRIS, where the electron radial spectral temperature was found to be 3-4 times higher than the axial one.

ACKNOWLEDGMENTS

This work is supported by Agence Nationale de la Recherche, with the contract # 21-ESRE-0018 EQUIPEX+ NEWGAIN. The authors are grateful to Tanguy Cadoux (CEA-Irfu) for providing the ASTERICS cold mass geometry, to Mile Kusulja and Francis Vezzu (CNRS-LPSC) for providing the ion source mechanics dimensions and images and Guillaume Brunet (GANIL) for the LEBT geometry.

DATA AVAILABILITY STATEMENT

The data that support the findings of this study are available from the corresponding author upon reasonable request.

¹T. Thuillier, J. Angot, J. Y. Benitez, A. Hodgkinson, C. M. Lyneis, D. S. Todd, and D. Z. Xie, "Investigation on the electron flux to the wall in the VENUS ion source," *Rev. Sci. Instrum.* **87**, 02A736 (2015), https://pubs.aip.org/aip/rsi/article-pdf/doi/10.1063/1.4935989/15842769/02a736_1_online.pdf.

²T. Thuillier *et al.*, "ASTERICS, a new 28 GHz electron cyclotron resonance ion source for the SPIRAL2 accelerator," *J. Phys. Conf. Ser.* **2743**, 012059 (2024).

³B. P. Cluggish, L. Zhao, and J.-S. Kim, "Modeling of the stability of electron cyclotron resonance ion source plasmas," *Nuclear Instruments and Methods in Physics Research Section A: Accelerators, Spectrometers, Detectors and Associated Equipment* **631**, 111–120 (2011).

⁴J. Benitez, C. Lyneis, L. Phair, D. Todd, and D. Xie, "Dependence of the Bremsstrahlung Spectral Temperature in Minimum-B Electron Cyclotron Resonance Ion Sources," *IEEE Trans. Plasma Sci.* **45**, 1746–1754 (2017).

- ⁵D. Neben, J. Fogleman, B. Isherwood, D. Leitner, G. Machicoane, S. Renteria, J. Stetson, and L. Tobos, “X-ray investigation on the Superconducting Source for Ions (SuSI),” *J. Instrum.* **14**, C02008 (2019).
- ⁶J. B. Li, L. X. Li, B. S. Bhaskar, V. Toivanen, O. Tarvainen, D. Hitz, L. B. Li, W. Lu, H. Koivisto, T. Thuillier, J. W. Guo, X. Z. Zhang, H. Y. Zhao, L. T. Sun, and H. W. Zhao, “Effects of magnetic configuration on hot electrons in a minimum-b ecr plasma,” *Plasma Phys. Controlled Fusion* **62**, 095015 (2020).
- ⁷A. Cernuschi and T. Thuillier, “Effect of magnetic configuration on hot electrons in a minimum-B ECR plasma,” To be submitted to *Phys. Rev. Accel. Beams*.
- ⁸O. Tarvainen, J. Laulainen, J. Komppula, R. Kronholm, T. Kalvas, H. Koivisto, I. Izotov, D. Mansfeld, and V. Skalyga, “Limitations of electron cyclotron resonance ion source performances set by kinetic plasma instabilities,” *Rev. Sci. Instrum.* **86**, 023301 (2015), https://pubs.aip.org/aip/rsi/article-pdf/doi/10.1063/1.4906804/15728790/023301_1_online.pdf.
- ⁹G. Battistoni, T. Boehlen, F. Cerutti, P. W. Chin, L. S. Esposito, A. Fassò, A. Ferrari, A. Lechner, A. Empl, A. Mairani, A. Mereghetti, P. G. Ortega, J. Ranft, S. Roesler, P. R. Sala, V. Vlachoudis, and G. Smirnov, “Overview of the fluka code,” *Ann. Nucl. Energy* **82**, 10–18 (2015), joint International Conference on Supercomputing in Nuclear Applications and Monte Carlo 2013, SNA + MC 2013. Pluri- and Trans-disciplinarity, Towards New Modeling and Numerical Simulation Paradigms.
- ¹⁰D. Simon *et al.*, “Design of ASTERICS: A superconducting 28 GHz ECR ion source magnet for GANIL,” *IEEE Trans. Appl. Supercond.* **33**, 4002905 (2023).
- ¹¹D. Leitner, J. Y. Benitez, C. M. Lyneis, D. S. Todd, T. Ropponen, J. Ropponen, H. Koivisto, and S. Gammino, “Measurement of the high energy component of the x-ray spectra in the venus electron cyclotron resonance ion source,” *Review of Scientific Instruments* **79**, 033302 (2008), https://pubs.aip.org/aip/rsi/article-pdf/doi/10.1063/1.2821137/13628624/033302_1_online.pdf.
- ¹²G. Gaudart, Thesis of Université Joseph Fourier, Grenoble, France (in French). #TS95-GREI-0197. (1995).
- ¹³M. Lamoureux, “Interest of electron–ion bremsstrahlung for plasma physics,” *Radiation Physics and Chemistry* **59**, 171–180 (2000).
- ¹⁴J. Noland, J. Y. Benitez, D. Leitner, C. Lyneis, and J. Verboncoeur, “Measurement of radial and axial high energy x-ray spectra in electron cyclotron resonance ion source plasmata,” *Review of Scientific Instruments* **81**, 02A308 (2010), https://pubs.aip.org/aip/rsi/article-pdf/doi/10.1063/1.3258614/13932028/02a308_1_online.pdf.
- ¹⁵M. Moscatello *et al.*, “NEWGAIN project at GANIL-SPIRAL2: design of the new heavy ion injector for the superconducting LINAC,” in *Proc. IPAC’23*, International Particle Accelerator Conference No. 14 (JACoW Publishing, 2023) pp. 1747–1749.